Journal of Sound and Vibration (2001) **244**(2), 211–233
doi:10.1006/jsvi.2000.3468, available online at http://www.idealibrary.com on IDEAL®

ON THE WAVEGUIDE MODELLING OF DYNAMIC STIFFNESS OF CYLINDRICAL VIBRATION ISOLATORS. PART I: THE MODEL, SOLUTION AND EXPERIMENTAL COMPARISON

L. KARI

MWL, Department of Vehicle Engineering, Kungliga Tekniska Högskolan, 100 44 *Stockholm, Sweden.*
E-mail: leifk@fkt.kth.se

(*Received* 10 *May* 1999, *and in final form* 5 *October* 2000)

A waveguide model of the axial dynamic stiffness for cylindrical vibration isolators in the audible frequency range is presented. The problems of satisfying the cylinder boundary conditions simultaneously are removed, by adopting the mode-matching technique, using the dispersion relation for an infinite cylinder and approximately satisfying the boundary conditions at the lateral surfaces by a circle-wise fulfilment or a subregion method. The rubber material is assumed to be nearly incompressible with deviatoric viscoelasticity based on a fractional order derivative model. The main advantage of the viscoelastic model is the minimum parameter number required to model the material properties successfully over a broad structure-borne sound frequency domain. The work is verified by experiments on a rubber cylinder, equipped with bonded circular steel plates, in the frequency range 100–5000 Hz. The model and the measurements are shown to agree strikingly well within the whole frequency range. Comparisons with alternative material models, known as the Kelvin–Voigt and frequency-independent or 'hysteric' material models, are made. The results are shown to diverge substantially from the presented material model; in particular, the Kelvin–Voigt model overestimates the material damping in the high-frequency region, while the frequency-independent model underestimates it. In addition, the resonance and anti-resonance frequencies are incorrectly predicted. In a companion paper the dispersion relation solution, convergence analysis and comparison with simple models are addressed.

1. INTRODUCTION

Structural vibrations at audible frequency range, that is structure-borne sound, radiate sound causing a major environmental problem. To reduce the transmitted structure-borne sound energy, thereby reducing noise pollution, the receiving structures are disconnected from the source by vibration isolators. The increased interest in noise abatement requires suitable models predicting transmitted sound through vibration isolators. Analytical models using the longitudinal modes in cylinders up to a few kHz are of particular interest. Although other isolator motions such as rotation or lateral motion may be important in some situations, the axial motion plays, in general, an important part in practical installations. An analytical model for the axial motion is, in addition, a valuable tool in its own right.

A different approach is through a numerical method, such as the finite element method (FEM), [1–3], or the boundary element method [4]. Although FEM handles arbitrary

0022-460X/01/270211 + 23 $35.00/0

geometry and difficult constitutive equations with great success, it is not ideal for modelling higher order modes, where they may be quite cumbersome in an iterative design process, while interpreting the results is usually difficult, as no closed form solution is obtained.

Increased complexity in analytically modelling wave propagation in finite cylinders is caused by difficulties in simultaneously satisfying boundary conditions at lateral and radial surfaces of the cylinder. An analytical and physically attractive method is the mode-matching technique. Zemanek [5] investigated longitudinal wave propagation in a solid cylinder by mode matching. Boundary conditions at the free lateral surface are satisfied pointwise by mode matching the incident and the reflected lowest order longitudinal mode, along with a finite number of higher order longitudinal modes with complex wave numbers with results verified by experiments on an aluminium cylinder. However, Zemanek considered only the lowest longitudinal mode as an incident wave. His analysis is, moreover, limited to elastic materials, that is, with no material damping.

Suitable constitutive relations including material damping are found in linear viscoelastic models. The classical example in materials for structure-borne sound analysis is the linear structural damping model with a frequency-independent loss factor [6]. This example, as pointed out by Crandall [7], exhibits non-causal behaviour, which is physically unrealistic. A physically more attractive description of the linear properties of real materials—including material damping—is by means of linear hereditary laws, expressed as convolution integrals [8]. However, the number of material constants required to describe rubber relaxation or creep properties successfully over a broad structure-borne sound frequency range are often large, resulting in a cumbersome number or a reduction of the frequency range. A major reduction with a preserved broad frequency range is obtained by fractional derivative models [9].

The aim is to model dynamic properties over a broad frequency range, up to at least 5000 Hz, expressed in terms of the axial driving point stiffness and the axial transfer stiffness, analytically derived by mode matching. Although strictly valid only for infinitesimal strains, it generates an improved understanding of the influences of higher order modes, losses and structure-borne sound dispersion. In a companion paper [10] the dispersion relation solution, convergence analysis and comparison with simple models are presented.

2. METHOD

2.1. NOTATIONS

Tensors are denoted by boldface and their components by lightface letters, repetition of indices is avoided as tensors rather than their components are employed. Tr, $^{\mathrm{T}}$, dev and div abbreviate trace, transpose, (symmetrized) deviation (or "shear") and divergence. The operators *, $\mathfrak{R}$ and $\mathfrak{I}$ denote complex conjugate, real part and imaginary part. Moreover, $\cdot$ denotes scalar product while $\mathbb{N}$ and $\mathbb{Z}_+$ are sets of natural numbers and of positive integers, respectively.

2.2. VIBRATION ISOLATOR

A typical example in Figure 1 consists of a vulcanized rubber cylinder firmly bonded to two parallel metal plates. Throughout, ρ and ρ_{mp} are the cylinder and plate densities, l is the cylinder length, l_{mp} is the plate thickness, a is the cylinder radius and $S = \pi a^2$ is the cylinder cross-sectional area with the radius equalling the plates radii.

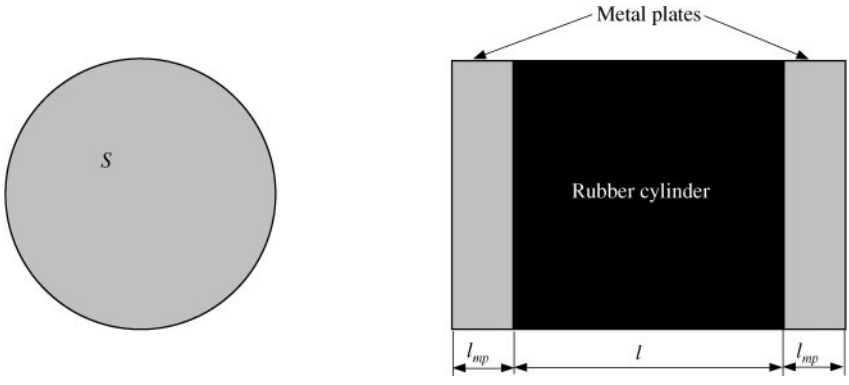

Figure. 1. Cylindrical vibration isolator.

2.3. CONSTITUTIVE ASSUMPTIONS

The rubber material is assumed to be isotropic, homogeneous, nearly incompressible and non-ageing, while obeying the principle of fading memory [8]. Since the focus of the study is the effect of higher order modes and dispersion, analysis is confined to isothermal conditions, infinitesimal strains and prestrains. Crystallization and non-linear friction are not considered. A convolution integral, expressed as a constitutive relaxation relation, is additively decomposed into a spherical (or "compression") part

$$\operatorname{tr}\sigma = 3\kappa_\infty \operatorname{div}\mathbf{u} + \int_{-\infty}^{t} 3\kappa_1(t-\tau)\,\frac{\partial \operatorname{div}\mathbf{u}(\tau)}{\partial\tau}\,\mathrm{d}\tau \tag{1}$$

and a deviatorical (or "shear") part

$$\operatorname{dev}\sigma = 2\mu_\infty \operatorname{dev}[\nabla\mathbf{u}] + \int_{-\infty}^{t} 2\mu_1(t-\tau)\,\frac{\partial \operatorname{dev}[\nabla\mathbf{u}(\tau)]}{\partial\tau}\,\mathrm{d}t, \tag{2}$$

where σ is the stress and $\mathbf{u}$ the displacement, with ∇ as the covariant derivative, Fung [11]. Compression and shear relaxation functions are additively decomposed as [8]

$$\kappa(t) = \kappa_\infty h(t) + \kappa_1(t), \qquad \mu(t) = \mu_\infty h(t) + \mu_1(t), \tag{3}$$

where $\lim_{t\to\infty}\kappa_1(t) = \lim_{t\to\infty}\mu_1(t) = 0$, h is the step function, $\kappa_\infty = \lim_{t\to\infty}\kappa(t)$ and $\mu_\infty = \lim_{t\to\infty}\mu(t)$ are the equilibrium elastic moduli. Temporal Fourier transformations, $\tilde{(\cdot)} = \int_{-\infty}^{\infty}(\cdot)\,\mathrm{e}^{-\mathrm{i}\omega t}\,\mathrm{d}t$, of the constitutive relaxation relations yield

$$\operatorname{tr}\tilde{\sigma} = 3\hat{\kappa}\operatorname{div}\tilde{\mathbf{u}} \tag{4}$$

and

$$\operatorname{dev}\tilde{\sigma} = 2\hat{\mu}\operatorname{dev}[\nabla\tilde{\mathbf{u}}], \tag{5}$$

where $\hat{\kappa}(\omega) = \kappa_\infty + \mathrm{i}\omega\tilde{\kappa}_1(\omega)$ and $\hat{\mu}(\omega) = \mu_\infty + \mathrm{i}\omega\tilde{\mu}_1(\omega)$ are the complex bulk and shear moduli, while ω is the angular frequency and i the imaginary unit.

In general, compression and shear relaxation functions are independent. However, a simple and suitable model for rubber material assumes that they are dependent as

$$\kappa(t) = b\mu_\infty h(t), \tag{6}$$

where the positive real-valued constant $b \gg 1$, typically $\sim 10^2$–10^5. This nearly incompressible example reduces equation (4) to

$$\text{tr}\,\tilde{\sigma} = 3b\mu_\infty \,\text{div}\,\tilde{\mathbf{u}}. \tag{7}$$

Helmholtz theorem, [11], gives $\mathbf{u} = \text{grad}\,\phi + \text{curl}\,\psi$, where ϕ and ψ are the scalar and vector potentials. Through the gauge transformation $\psi' = \psi - \text{grad}\,\phi'$, where $\text{div}\,\psi' = 0$, the Helmholtz equations become

$$\nabla^2\tilde{\phi} + k_L^2\tilde{\phi} = 0 \quad \text{and} \quad \nabla^2\tilde{\psi}' + k_T^2\tilde{\psi}' = 0, \tag{8, 9}$$

where ∇^2 is the Laplacean; k_L and k_T are the longitudinal and transversal wave number, respectively. They read

$$k_L = \omega\sqrt{\frac{\rho}{b\mu_\infty}\,\frac{1}{1 + 4\hat{\mu}/3b\mu_\infty}} \quad \text{and} \quad k_T = \omega\sqrt{\frac{\rho}{\hat{\mu}}}, \tag{10a, b}$$

for the nearly incompressible model. In contrast to a synchronous material model (that is, $\kappa(t) = b\mu(t)$) with $b \gg 1$, the loss factor for the longitudinal wave number is not normally overestimated.

2.4. FORMULATION OF THE GENERAL PROBLEM

A practical field representation at the junctions of the plates and mounting structures is by variables acting at the junction centres. In Figure 2, the stress field is represented by the force and moment vectors, with the displacement field represented by the displacement and rotation vectors. As this is the vibration isolator dynamic stiffness description, only rigid body motions of the junctions at 1 and 2 are allowed. The plates are modelled as rigid. A suitable description of the vibration isolators structure-borne sound properties provides the blocked dynamic axial driving point and transfer stiffness, defined as

$$\tilde{k}_{11} = \tilde{\mathbf{f}}\cdot\mathbf{n}|_1/\tilde{\mathbf{d}}\cdot\mathbf{n}|_1 \quad \text{and} \quad \tilde{k}_{12} = \tilde{\mathbf{f}}\cdot\mathbf{n}|_2/\tilde{\mathbf{d}}\cdot\mathbf{n}|_1, \tag{11, 12}$$

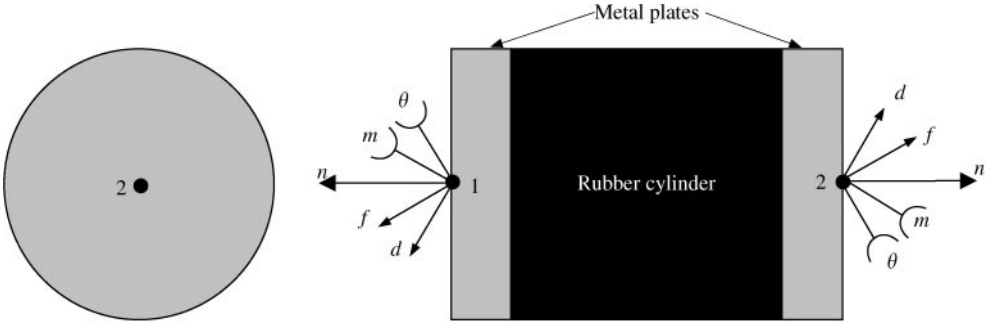

Figure. 2. Representation of fields. The unit outward normal to the junction is denoted **n**, while **d**, **f**, **m** and θ are the displacement, force, moment and rotation vectors.

provided junction 2 is blocked; $\tilde{\mathbf{d}}|_2 = \tilde{\theta}|_2 = \mathbf{0}$, and that only axial displacement exists on junction 1; $\tilde{\mathbf{d}} - (\tilde{\mathbf{d}}\cdot\mathbf{n})\mathbf{n}|_1 = \tilde{\theta}|_1 = \mathbf{0}$, $\tilde{\mathbf{d}}|_1 \neq \mathbf{0}$. In addition,

$$\tilde{k}_{22} = \tilde{\mathbf{f}}\cdot\mathbf{n}|_2/\tilde{\mathbf{d}}\cdot\mathbf{n}|_2 \quad \text{and} \quad \tilde{k}_{21} = \tilde{\mathbf{f}}\cdot\mathbf{n}|_1/\tilde{\mathbf{d}}\cdot\mathbf{n}|_2, \tag{13, 14}$$

provided junction 1 is blocked; $\tilde{\mathbf{d}}|_1 = \tilde{\theta}|_1 = \mathbf{0}$, and that only axial displacement exists on junction 2; $\tilde{\mathbf{d}} - (\tilde{\mathbf{d}}\cdot\mathbf{n})\mathbf{n}|_2 = \tilde{\theta}|_2 = \mathbf{0}$, $\tilde{\mathbf{d}}|_2 \neq \mathbf{0}$. Reciprocity implies $\tilde{k}_{21} = \tilde{k}_{12}$ and the particular vibration isolator symmetry $\tilde{k}_{22} = \tilde{k}_{11}$, which are subsequently used. Through similar procedures other components of dynamic stiffness are defined.

Consider the vibration isolator cylinder in Figure 3, a simple body consisting of continuously distributed rubber material and occupying a fixed set $\mathscr{B} \subset \mathbb{R}^3$ where fixed $\mathscr{B}$ defines the cylinder reference configuration, in its natural state; stress-free and undeformed. Let $\mathbf{u}$ and σ be the usual (spatial point dependent) displacement and stress. The mixed boundary conditions, in the frequency domain, are the displacements

$$\tilde{\mathbf{u}} = \tilde{\mathbf{d}}|_1 \quad \text{given on } \partial_d^1\mathscr{B}, \tag{15}$$

$$\tilde{\mathbf{u}} = \mathbf{0} \quad \text{given on } \partial_d^2\mathscr{B} \tag{16}$$

and, the traction

$$\tilde{\sigma}\mathbf{n} = \mathbf{0} \quad \text{given on } \partial_t\mathscr{B}, \tag{17}$$

where $\tilde{\mathbf{d}} - (\tilde{\mathbf{d}}\cdot\mathbf{n})\mathbf{n}|_1 = \mathbf{0}$, $\tilde{\mathbf{d}}|_1 \neq \mathbf{0}$, $\overline{\partial_d^1\mathscr{B}\cup\partial_d^2\mathscr{B}\cup\partial_t\mathscr{B}} = \partial\mathscr{B}$, $\partial\mathscr{B}$ is the boundary of the cylinder, $\partial\mathscr{B}$ its boundary closure and $\mathbf{n}$ is the unit outward normal to $\partial\mathscr{B}$. In addition, all the involved fields must be single-valued. It should be noted that there are stress singularities at the rubber cylinder corners $\overline{\partial_d^1\mathscr{B}}\cap\overline{\partial_t\mathscr{B}}$ and $\overline{\partial_d^2\mathscr{B}}\cap\overline{\partial_t\mathscr{B}}$, shown in Figure 3.

The dynamic stiffness becomes

$$\tilde{k}_{11} = \left[\int_{\partial_d^1\mathscr{B}} \mathbf{n}\cdot(\tilde{\boldsymbol{\sigma}}\mathbf{n})\,\mathrm{d}S - \omega^2\pi a^2 l_{mp}\rho_{mp}\tilde{\mathbf{d}}\cdot\mathbf{n}|_1\right]/\tilde{\mathbf{d}}\cdot\mathbf{n}|_1 \tag{18}$$

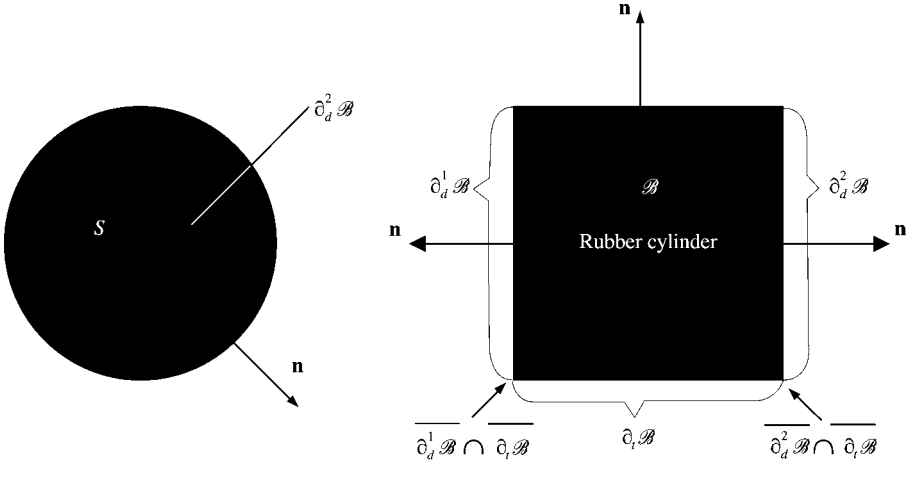

Figure. 3. Rubber cylinder. Mixed boundary condition. The steel plates are removed, compare with Figure 2.

and

$$\tilde{k}_{12} = \int_{\partial_d^2 \mathscr{B}} \mathbf{n} \cdot (\tilde{\sigma}\mathbf{n})\, \mathrm{d}S / (\tilde{\mathbf{d}} \cdot \mathbf{n}|_1), \tag{19}$$

provided rigid body motions of the metal plate, $\tilde{\mathbf{d}} - (\tilde{\mathbf{d}} \cdot \mathbf{n})\,\mathbf{n}|_1 = \tilde{\mathbf{u}}|_{\partial_d^2 \mathscr{B}} = \mathbf{0}$ and that $\tilde{\mathbf{d}}|_1 \neq \mathbf{0}$ where $\tilde{\sigma}$ is related to $\tilde{\mathbf{u}}$ by equations (5) and (7).

Formal derivation of the closed-form solution to this problem is laborious, on account of the singularities, the constitutive equation form and the imposed boundary conditions. In addition, boundary conditions on $\partial_d^1 \mathscr{B}$ and $\partial_d^2 \mathscr{B}$ are locally non-mixed, which refers to the problem of a non-separable nature. Miklowitz [12] discusses separability and non-separability in reference to elastic waves in solids.

The widely used technique of mode matching [13], is probably the most forthright method of solving this problem, where the axial dependence is separated and the remaining problem is solved, resulting in the eigenmodes of the cross-section. Finally, provided these functions constitute a complete set, the total field is obtained by superposition of the eigenmodes then matching them to the boundary conditions on $\partial_d^1 \mathscr{B}$ and $\partial_d^2 \mathscr{B}$.

2.5. DERIVATION OF EIGENVALUES AND EIGENMODES

Consider the infinite cylinder in Figure 4 where a convenient representation of the geometry is in a cylindrical co-ordinate system with the z-axis directed along the main axis. The axial dependence is readily separated by assuming an $\propto \exp(-\mathrm{i}\, k_z\, z)$ dependence for the field variables, where k_z is the axial wave number. Then, the relations (8), (9), (17), the Helmholtz theorem, the gauge transformation together with the requirements of single valuedness and non-singularity, result in a general transcendental equation. With respect to the original problem, only the axially symmetric and non-torsional part is important, due to boundary conditions (15) and (16). The particular transcendental equation reads

$$[k_T^2 - 2k_{\perp T}^2]^2 \vartheta(k_{\perp L} a) + 4k_{\perp L}^2 [k_T^2 - k_{\perp T}^2] \vartheta(k_{\perp T} a) = 2k_{\perp L}^2 k_T^2, \tag{20}$$

where

$$\vartheta = x \mathrm{J}_0(x) / \mathrm{J}_1(x), \tag{21}$$

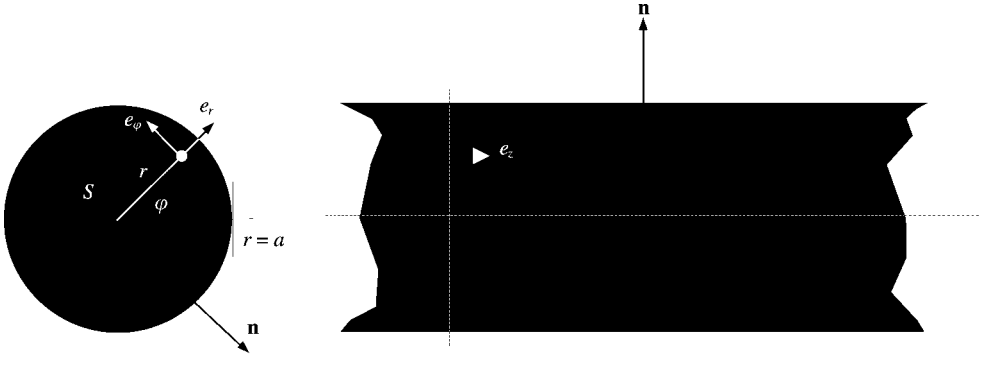

Figure. 4. Geometry of infinite rubber cylinder.

also known as the Onoe function of the first kind and first order, and J_n is the Bessel function of the first kind and order n. The axial wave number is given by

$$k_{\perp L}^2 = k_L^2 - k_z^2 \tag{22}$$

or

$$k_{\perp T}^2 = k_T^2 - k_z^2. \tag{23}$$

An elaborated derivation of equation (20) together with equations (21)–(23), restricted to elastic materials, is given in standard textbooks, such as Graff [14], Pochhammer [15] and Chree [16].

The relations (20)–(23) constitute the dispersion relation

$$k_{z,n} = k_{z,n}(\omega), \tag{24}$$

for the eigenmodes of the infinite cylinder, where $n \in \mathbb{Z}_+$ and labels different solutions; the eigenvalues $k_{z,n}$, $k_{\perp L,n}$ and $k_{\perp T,n}$. As the transcendental equation is an even function of k_z, $k_{\perp L}$ and $k_{\perp T}$, $-k_z$, $-k_{\perp L}$ and $-k_{\perp T}$ are also solutions. Therefore, it is sufficient to be restricted to $\Re\, k_z \geqslant 0$, $\Re\, k_{\perp L} \geqslant 0$ and $\Re\, k_{\perp T} \geqslant 0$. In addition, the stiffness obeys $\tilde{k}_{11}(-\omega) = \tilde{k}_{11}^*(\omega)$ and $\tilde{k}_{12}(-\omega) = \tilde{k}_{12}^*(\omega)$, due to the properties of a temporal Fourier transform. As a result, it is sufficient to consider $k_{z,n} = k_{z,n}(\omega)$ restricted to $\omega \geqslant 0$ and $\Re\, k_{z,n} \geqslant 0$. The continuation to $\Re\, k_{z,n} < 0$ is performed by the formal replacement of $k_{z,n} \leftarrow -k_{z,n}$.

Finally, in terms of the potential physical components, the sufficient and somewhere non-vanishing eigenmodes are, [14], the scalar potential

$$\tilde{\phi}_n \propto J_0(k_{\perp L,n} r) \tag{25}$$

and the φ-component of the vector potential

$$\tilde{\psi}_{\varphi,n} \propto J_1(k_{\perp T,n} r), \tag{26}$$

$r \in [0, a]$, with the corresponding eigenvalues $k_{\perp L,n}$ and $k_{\perp T,n}$, respectively.

2.6. DERIVATION OF DYNAMIC STIFFNESS

Consider again the finite vibration isolator, where the geometry is represented in a cylindrical co-ordinate system with the z-axis directed along the main axis, as shown in Figure 5. Arbitrary axially symmetric and non-torsional stress and strain fields are obtained by superposition of the eigenmodes derived above, provided these functions constitute a complete set. In the case of elastic materials, Love [17] points out that the real eigenvalues are finite in number at a given frequency, thus the corresponding eigenfunctions cannot themselves form a complete set. Likewise, the purely imaginary eigenvalues are finite in number at a given frequency. However, Adem [18] shows that there are also an infinite number of complex eigenvalues at a given frequency, rendering a complete set possible. The completeness extension to viscoelastic materials is provided by analytical continuation. For the mathematical grounds concerning waveguide solutions, the reader may refer to Cessenat [19] or [13]. Thus, the following expressions can be formulated for the potential

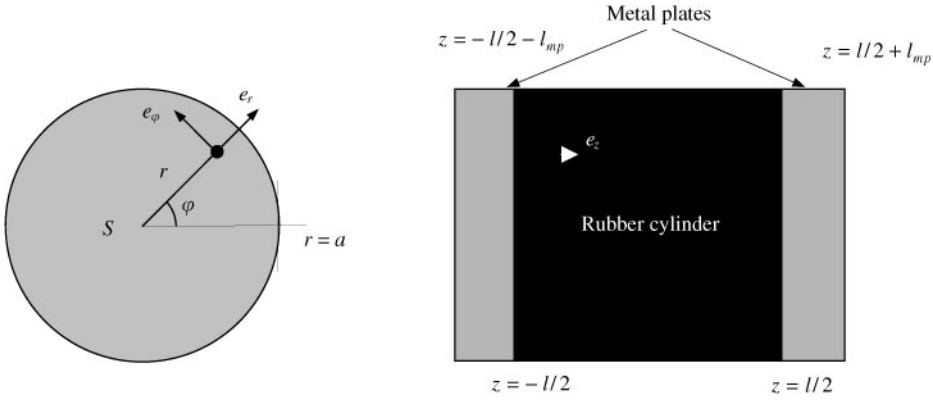

Figure. 5. Geometry of the cylindrical vibration isolator.

fields within the finite cylinder:

$$\tilde{\phi} = \sum_{n=1}^{\infty} [A_n^+ \, \mathrm{e}^{-\mathrm{i}k_{z,n}z} + A_n^- \, \mathrm{e}^{\mathrm{i}k_{z,n}z}] \, \mathrm{J}_0(k_{\perp L,n} r) \tag{27}$$

and

$$\tilde{\psi}_\varphi = \sum_{n=1}^{\infty} [B_n^+ \, \mathrm{e}^{-\mathrm{i}k_{z,n}z} + B_n^- \, \mathrm{e}^{\mathrm{i}k_{z,n}z}] \, \mathrm{J}_1(k_{\perp T,n} r), \tag{28}$$

where $r \in [0, a[$ and $z \in]-l/2, l/2[$, with (Helmholtz theorem) $\tilde{\mathbf{u}} = \mathrm{grad}\ \tilde{\phi} + \mathrm{curl}\ \tilde{\psi}$ and $\tilde{\sigma}$ is related to $\tilde{\mathbf{u}}$ by equations (5) and (7). The coefficients are interrelated as $A_n^+ = P_n B_n^+$ and $A_n^- = -P_n B_n^-$, where

$$P_n = \frac{k_{\perp T,n}^2 - k_{z,n}^2 \mathrm{J}_1(k_{\perp T,n} a)}{2\mathrm{i}k_{\perp L,n} k_{z,n} \mathrm{J}_1(k_{\perp L,n} a)}, \tag{29}$$

because of the boundary condition (17). The boundary condition (15) becomes, with equations (27)–(29) and Helmholtz theorem,

$$\sum_{n=1}^{\infty} [C_n^+ \, \mathrm{e}^{\mathrm{i}k_{z,n}l/2} + C_n^- \, \mathrm{e}^{-\mathrm{i}k_{z,n}l/2}] \, U_n^r = 0 \tag{30}$$

and

$$\sum_{n=1}^{\infty} [C_n^+ \, \mathrm{e}^{\mathrm{i}k_{z,n}l/2} - C_n^- \, \mathrm{e}^{-\mathrm{i}k_{z,n}l/2}] \, U_n^z = -\tilde{d}^z, \tag{31}$$

where

$$U_n^r = -k_{\perp L,n}[k_{\perp T,n}^2 - k_{z,n}^2] \, \mathrm{J}_1(k_{\perp T,n} a) \, \mathrm{J}_1(k_{\perp L,n} r) - 2k_{\perp L,n} k_{z,n}^2 \, \mathrm{J}_1(k_{\perp L,n} a) \, \mathrm{J}_1(k_{\perp T,n} r), \tag{32}$$

$$U_n^z = -\mathrm{i}k_{z,n}[k_{\perp T,n}^2 - k_{z,n}^2] \, \mathrm{J}_1(k_{\perp T,n} a) \, \mathrm{J}_0(k_{\perp L,n} r) + 2\mathrm{i}k_{\perp L,n} \, k_{\perp T,n} k_{z,n} \, \mathrm{J}_1(k_{\perp L,n} a) \, \mathrm{J}_0(k_{\perp T,n} r), \tag{33}$$

$C_n^+ X_n = B_n^+$, $-C_n^- X_n = B_n^-$, $X_n = 2\mathrm{i}k_{\perp L,n}k_{z,n}\,\mathrm{J}_1(k_{\perp L,n}a)$ and $r \in [0, a]$. The boundary condition (16) reads

$$\sum_{n=1}^{\infty} [C_n^+ \,\mathrm{e}^{-\mathrm{i}k_{z,n}l/2} + C_n^- \,\mathrm{e}^{\mathrm{i}k_{z,n}l/2}]\, U_n^r = 0 \tag{34}$$

and

$$\sum_{n=1}^{\infty} [C_n^+ \,\mathrm{e}^{-\mathrm{i}k_{z,n}l/2} - C_n^- \,\mathrm{e}^{\mathrm{i}k_{z,n}l/2}]\, U_n^z = 0, \tag{35}$$

where $r \in [0, a]$.

The most straightforward way to obtain the coefficients from the relations (30)–(35) is probably through the point-matching technique but in most cases, more accurate results are achieved by the subregion method, which is a generalization of point matching.

2.6.1. *Point-matching method*

This represents the domain by specific points. Due to the axisymmetry of the problem, each point may be extended in Figure 6 to axisymmetric circles. In particular, the lateral boundaries $\partial_d^k \mathscr{B}$ are represented by the circles; $r \in \{{}_r^k r_1,\ {}_r^k r_2, \ldots, {}_r^k r_{P_r^k}\}$ and $r \in \{{}_z^k r_1,\ {}_z^k r_2, \ldots, {}_z^k r_{P_z^k}\}$; $\varphi \in [0, 2\pi[$ and $z = -l/2$ $(k = 1)$ or $z = l/2$ $(k = 2)$, where $0 \neq {}_r^k r_1 < {}_r^k r_2 < \ldots < {}_r^k r_{P_r^k}$, ${}_z^k r_1 < {}_z^k r_2 < \ldots < {}_z^k r_{P_z^k}$ and $P_r^k,\ P_z^k \in \mathbb{N}$. The indices r and z refer to boundary conditions in r and z directions. The separation into the two directions is carried out to retain maximum flexibility. The boundary conditions are replaced by circle-wise fulfilment. To obtain a finite number of equations, the series in equations (30)–(35), must, preceding point matching, be truncated after M terms, where $P_r^1 + P_z^1 + P_r^2 + P_z^2 \geqslant 2M \in \mathbb{Z}_+$. Thus, the boundary conditions (30)–(35) are replaced by

$$\sum_{n=1}^{M} [D_n^+ \,\mathrm{e}^{\mathrm{i}k_{z,n}l/2} + D_n^- \,\mathrm{e}^{-\mathrm{i}k_{z,n}l/2}]\, U_n^r({}_r^1 r_j) = 0, \tag{36}$$

$$\sum_{n=1}^{M} [D_n^+ \,\mathrm{e}^{\mathrm{i}k_{z,n}l/2} - D_n^- \,\mathrm{e}^{-\mathrm{i}k_{z,n}l/2}]\, U_n^z({}_z^1 r_m) = -1, \tag{37}$$

$$\sum_{n=1}^{M} [D_n^+ \,\mathrm{e}^{-\mathrm{i}k_{z,n}l/2} + D_n^- \,\mathrm{e}^{\mathrm{i}k_{z,n}l/2}]\, U_n^r({}_r^2 r_j) = 0 \tag{38}$$

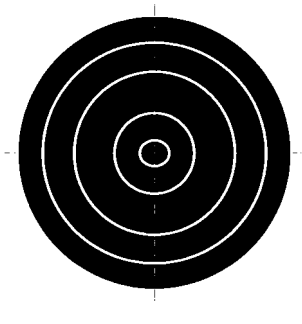

Figure. 6. Collocation circles at lateral boundary.

and

$$\sum_{n=1}^{M} [D_n^+ \, \mathrm{e}^{-\mathrm{i}k_{z,n}l/2} - D_n^- \, \mathrm{e}^{\mathrm{i}k_{z,n}l/2}] \, U_n^z({}_r^2 r_m) = 0, \tag{39}$$

where $D_n^+ \tilde{d} = C_n^+$, $D_n^- \tilde{d} = C_n^-$, $j = 1, 2, \ldots, P_r^k$ and $m = 1, 2, \ldots, P_z^k$.

2.6.2. *Subregion method*

This method subdivides the domain into subdomains. In particular, the lateral boundaries may be divided into sub-boundaries as

$$\overline{\partial_d^k \mathscr{B}} = \overline{\bigcup_{j1}^{P_r^k} \partial_{d,r}^{k,j} \mathscr{B}} = \overline{\bigcup_{m.1}^{P_z^k} \partial_{d,z}^{k,m} \mathscr{B}}, \tag{40}$$

where P_r^k, $P_z^k \in \mathbb{N}$ and $k = 1, 2$. The indices r and z refer to boundary conditions in r and z directions. Moreover, the pointwise fulfilment of the boundary conditions is replaced by equality in the mean, by integration over each sub-boundary. To obtain a finite number of equations, the series in equations (30)–(35), must, preceding the subregion method, be truncated after M terms, where $P_r^1 + P_z^1 + P_r^2 + P_z^2 \geqslant 2M \in \mathbb{Z}_+$. The boundary conditions are replaced by

$$\sum_{n=1}^{M} \int_{\partial_{d,r}^{1,j}\mathscr{B}} [C_n^+ \, \mathrm{e}^{\mathrm{i}k_{z,n}l/2} + C_n^- \, \mathrm{e}^{-\mathrm{i}k_{z,n}l/2}] \, U_n^r \, \mathrm{d}S = 0, \tag{41}$$

$$\sum_{n=1}^{M} \int_{\partial_{d,z}^{1,m}\mathscr{B}} [C_n^+ \, \mathrm{e}^{\mathrm{i}k_{z,n}l/2} - C_n^- \, \mathrm{e}^{-\mathrm{i}k_{z,n}l/2}] \, U_n^z \, \mathrm{d}S = - \int_{\partial_{d,z}^{1,m}\mathscr{B}} \tilde{d} \, \mathrm{d}S, \tag{42}$$

$$\sum_{n=1}^{M} \int_{\partial_{d,r}^{2,j}\mathscr{B}} [C_n^+ \, \mathrm{e}^{-\mathrm{i}k_{z,n}l/2} + C_n^- \, \mathrm{e}^{\mathrm{i}k_{z,n}l/2}] \, U_n^r \, \mathrm{d}S = 0 \tag{43}$$

and

$$\sum_{n=1}^{M} \int_{\partial_{d,z}^{2,m}\mathscr{B}} [C_n^+ \, \mathrm{e}^{-\mathrm{i}k_{z,n}l/2} - C_n^- \, \mathrm{e}^{\mathrm{i}k_{z,n}l/2}] \, U_n^z \, \mathrm{d}S = 0, \tag{44}$$

where $j = 1, 2, \ldots, P_r^k$ and $m = 1, 2, \ldots, P_z^k$. Due to the axisymmetry of the problem, sub-boundaries $\partial_{d,r}^{k,j}\mathscr{B}$ and $\partial_{d,z}^{k,m}\mathscr{B}$ are readily represented by the surfaces; $r \in [{}_r^k r_{j-1}, {}_r^k r_j]$ and $r \in [{}_z^k r_{m-1}, {}_z^k r_m]$, $\varphi \in [0, 2\pi[$ and $z = -l/2$ ($k = 1$) or $z = l/2$ ($k = 2$), where $0 = {}_r^k r_0 < {}_r^k r_1 < \ldots < {}_r^k r_{P_r{}^k} = a$, ($P_r^k \neq 0$), and $0 = {}_z^k r_0 < {}_z^k r_1 < \ldots < {}_z^k r_{P_z{}^k} = a$, ($P_z^k \neq 0$).

By using the relations $\int x \, \mathrm{J}_0(x) \, \mathrm{d}x = x \, \mathrm{J}_1(x)$ and $\int x \, \mathrm{J}_1(x) \, \mathrm{d}x = \pi x [\Xi_0(x) \, \mathrm{J}_1(x) - \Xi_1(x) \, \mathrm{J}_0(x)]/2$, where Ξ_n is a Struve function of order n, defined in reference [20], the boundary conditions (41)–(44) read

$$\sum_{n=1}^{M} [D_n^+ \, \mathrm{e}^{\mathrm{i}k_{z,n}l/2} + D_n^- \, \mathrm{e}^{-\mathrm{i}k_{z,n}l/2}] [Y_n^r({}_r^1 r_j) - Y_n^r({}_r^1 r_{j-1})] = 0, \tag{45}$$

$$\sum_{n=1}^{M} [D_n^+ \mathrm{e}^{\mathrm{i}k_{z,n}l/2} - D_n^- \, \mathrm{e}^{-\mathrm{i}k_{z,n}l/2}] [Y_n^z({}_z^1 r_m) - Y_n^z({}_z^1 r_{m-1})] = \pi [{}_z^1 r_{m-1}^2 - {}_z^1 r_m^2], \tag{46}$$

$$\sum_{n=1}^{M} [D_n^+ \, \mathrm{e}^{-\mathrm{i}k_{z,n}l/2} + D_n^- \, \mathrm{e}^{\mathrm{i}k_{z,n}l/2}] [Y_n^r({}_r^2 r_j) - Y_n^r({}_r^2 r_{j-1})] = 0 \tag{47}$$

and

$$\sum_{n=1}^{M} [D_n^+ \, \mathrm{e}^{-\mathrm{i}k_{z,n}l/2} - D_n^- \, \mathrm{e}^{\mathrm{i}k_{z,n}l/2}][Y_n^z(_z^2 r_m) - Y_n^z(_z^2 r_{m-1})] = 0, \tag{48}$$

where

$$Y_n^r = \pi^2 r \left[[k_{\perp T,n}^2 - k_{z,n}^2] \, \mathrm{J}_1(k_{\perp T,n} a) \, W(k_{\perp L,n} r) + 2 \frac{k_{\perp L,n}}{k_{\perp T,n}} k_{z,n}^2 \, \mathrm{J}_1(k_{\perp L,n} a) \, W(k_{\perp T,n} r) \right], \tag{49}$$

$$Y_n^z = 2\pi r \left[-\mathrm{i} \frac{k_{z,n}}{k_{\perp L,n}} [k_{\perp T,n}^2 - k_{z,n}^2] \, \mathrm{J}_1(k_{\perp T,n} a) \, \mathrm{J}_1(k_{\perp L,n} r) + 2\mathrm{i} k_{\perp L,n} k_{z,n} \, \mathrm{J}_1(k_{\perp L,n} a) \, \mathrm{J}_1(k_{\perp T,n} r) \right], \tag{50}$$

$W = J_0 \Xi_1 - J_1 \Xi_0$, $D_n^+ \tilde{d} = C_n^+$, $D_n^- \tilde{d} = C_n^-$, $j = 1, 2, \ldots, P_r^k$ and $m = 1, 2, \ldots, P_z^k$.

2.6.3. *Dynamic stiffness*

The relations (36)–(39) and (45)–(48) may be written as $\mathbf{A}\mathbf{x} = \mathbf{b}$ where $\mathbf{A}$ is a known $[P_r^1 + P_z^1 + P_r^2 + P_z^2] \times 2M$ system matrix, $\mathbf{x}$ is an unknown coefficient vector $(D_1^+, D_1^-, D_2^+, D_2^-, \ldots, D_M^+, D_M^-)^{\mathrm{T}}$ and $\mathbf{b}$ is a known vector $(\underbrace{0, 0, \ldots, 0}_{P_r^1}, \underbrace{-1, -1, \ldots, -1}_{P_z^1}, \underbrace{0, 0, \ldots, 0}_{P_r^2 + P_z^2})^{\mathrm{T}}$ and $(\underbrace{0, 0, \ldots, 0}_{P_r^1}, \underbrace{\pi[r_0^2 - r_1^2], \pi[r_1^2 - r_2^2], \ldots, \pi[r_{P_z^1-1}^2 - r_{P_z^1}^2]}_{P_z^1}, \underbrace{0, 0, \ldots, 0}_{P_r^2 + P_z^2})^{\mathrm{T}}$, respectively.

Frequently, the rank of the system matrix is not numerically well determined so the problem of solving the equation may be ill-conditioned, especially for large values of $2M[P_r^1 + P_z^1 + P_r^2 + P_z^2]$. Moreover, the elements of $\mathbf{A}$ cover a wide range, mainly due to the exponential functions, frequently causing over- and underflow exceptions in subsequent computations. To increase the effective rank of the system matrix, the original system is rescaled and equilibrated into $\mathbf{A}'\mathbf{x}' = \mathbf{b}'$, where $\mathbf{A}' = \mathbf{D}_2\mathbf{A}\mathbf{D}_1$, $\mathbf{x} = \mathbf{D}_1\mathbf{x}'$, $\mathbf{b}' = \mathbf{D}_2\mathbf{b}$, $\mathbf{D}_1$ is $(2M \times 2M)$ diagonal scaling matrix and $\mathbf{D}_2$ is $[P_r^1 + P_z^1 + P_r^2 + P_z^2] \times [P_r^1 + P_z^1 + P_r^2 + P_z^2]$ diagonal scaling matrix. To avoid rounding off errors introduced by the scaling, the elements of the diagonal matrix are integer powers of the base in the number system used. Normally, the base is 2. At the equilibration, the maximum norm of each row and column of $\mathbf{A}'$ is set as equal as is possible. In practice, any ill-conditioning of $\mathbf{A}$ is then concentrated within the diagonal scaling. The effective rank of $\mathbf{A}'$ is determined by treating as zero those singular values which are less than the largest singular value times the floating point relative accuracy used. This accuracy equals 2^{-52} on machines with IEEE—arithmetic, roughly 2.22×10^{-16}. The equation system is solved by singular-value decomposition of the system matrix, which with the condition $\min \|\mathbf{A}'\mathbf{x}' - \mathbf{b}'\|_2$ in addition to a full rank of system matrix, also guarantees a unique solution.

The dynamic stiffness (18) and (19) becomes, using for example, $\tilde{\mathbf{u}} = \mathrm{grad}\, \tilde{\phi} + \mathrm{curl}\, \tilde{\psi}$, equations (27)–(29), (5), (7), (10), (22)–(23) and (36)–(39) or (45)–(48),

$$\tilde{k}_{11} = \pi a \omega^2 \left[2\rho \sum_{n=1}^{M} [D_n^+ \, \mathrm{e}^{\mathrm{i}k_{z,n}l/2} + D_n^- \, \mathrm{e}^{-\mathrm{i}k_{z,n}l/2}] \, S_n^{zz} - a l_{mp} \rho_{mp} \right] \tag{51}$$

and

$$\tilde{k}_{12} = 2\pi a\rho\omega^2 \sum_{n=1}^{M} [D_n^+ \, \mathrm{e}^{-\mathrm{i}k_{z,n}l/2} + D_n^- \, \mathrm{e}^{\mathrm{i}k_{z,n}l/2}] \, S_n^{zz}, \tag{52}$$

$$S_n^{zz} = [2k_{\perp L,n}^2 - k_{\perp T,n}^2 + k_{z,n}^2] \, \mathrm{J}_1(k_{\perp L,n}\, a) \, \mathrm{J}_1(k_{\perp T,n}\, a)/k_{\perp L,n}. \tag{53}$$

To summarize, point matching and subregion methods given above exactly satisfy the equations of motion and the traction free boundary condition. Regarding the displacement boundary conditions, point matching fulfils the conditions at circles and the subregion method fulfils conditions in the mean within two subsequent circles, provided the equation systems are exactly determined, that is, $P_r^1 + P_z^1 + P_r^2 + P_z^2 = 2M$ and the rank of $\mathbf{A}$ (or $\mathbf{A}'$) is $2M$. Inasmuch as the series (27) and (28) fully represent the potential fields within the cylinder, the expressions (51) and (52) model the dynamic stiffness to any desired accuracy for a sufficient number of eigenmodes.

3. RESULTS AND DISCUSSION

To examine the methods in practice, a real vibration isolator has been analyzed, presenting numerical as well as measurement results. The formulations given above are implemented on a PC - Pentium Pro®. The computer code is written in LAHEY FORTRAN 90® with all calculations performed in double precision. Graphically, the results are presented by means of MATLAB®.

3.1. TEST OBJECT

The test object is a compression moulded cylindrical vibration isolator $l = 50{\cdot}0$ mm long and $a = 50{\cdot}0$ mm radius, equipped with circular plates 2·6 mm thick and $a = 50{\cdot}0$ mm radius, in steel alloy SS 141312 cured to the rubber cylinder using superior bonding agents Tixon P6.1 and 520. In order to facilitate safe mounting, additional plates 19·0 mm thick and $a = 50{\cdot}0$ mm radius are attached with Hottinger Baldwin Messtechnik GmBH bonding agent X 60 having M 12 threaded centre holes. Total plate thickness is $l_{mp} = 21{\cdot}6$ mm. The rubber material is vulcanized natural rubber, filled with small amounts of non-reinforcing carbon black. The principal ingredients are given in Table 1. The nominal hardness is 40° IRH and the density 1050 kg/m^3. Maximum long-term axial static pre-load is limited to 3000 N.

3.2. MEASUREMENT OF DYNAMIC STIFFNESS AND MATERIAL PROPERTIES

3.2.1. *Measurement method*

The vibration isolator axial dynamic transfer stiffness is measured by an indirect method in Figure 7 with the isolator mounted between a block and the moving table of an electro-dynamic vibration generator membrane. The moving table and block motions are measured by piezo-electric accelerometers. The acceleration and mass of the block multiplied, supplies the blocking force needed for the transfer stiffness estimation. Data collection is performed by a 4-channel frequency analyzer, also supplying the signal to the generator via an amplifier with measurements processed by a personal computer. The instruments needed are tabulated in Table 2.

TABLE 1

Principal ingredients of the natural rubber compound

Category	Ingredient	Type	Concentration (phr)
Polymer	Natural rubber	SMR CV50	100
Filler system	Carbon black	N772	10
Stabilizer system	Antidegradant system	Antiozonant	1
		Antioxidant	1
		Wax	1
Vulcanization system components	Activators	Stearic acid	1
		Zinc oxide	5
	Vulcanizing agent	Sulphur	3
	Accelerator	CBS	2
Special materials	Processing oils	Paraffinic	1
		Aromatic	5

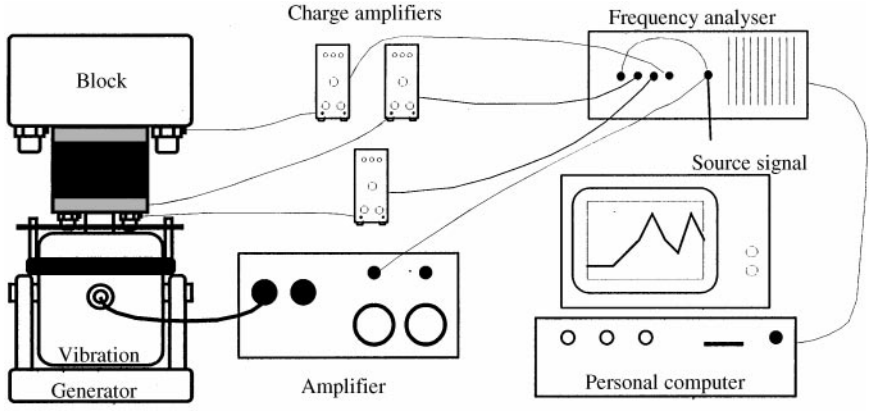

Figure. 7. Measurement set-up.

TABLE 2

Measurement instruments

Instrument	Type	Number
Electro-dynamic vibration generator	LDS V409	1
Amplifier	Labgruppen SS1400	1
Accelerometer	B&K 4393	2
Accelerometer	B&K 4367	3
Accelerometer	Rion PV-84	2
Charge amplifier	B&K 2635	3
Frequency analyzer	Tektronix 2630	1
Computer	Aquila PC486	1

Within the frequency range considered the block mass sufficiently reduces the motion of the block. Then axial dynamic transfer stiffness $\tilde{k}_{12} \approx \omega^2 m_b \tilde{u}_b / \tilde{u}_{mt}$, where $|\tilde{u}_b/\tilde{u}_{mt}| \ll 1$; m_b and u_b are the mass and the displacement of the block and u_{mt} is the displacement of the moving table.

In order to suppress (unwanted) rigid and non-rigid body motion influences, accelerometers are positioned symmetrically close to the isolator at several places on each block and on the moving table.

Let the frequency response function $\tilde{h}(\tilde{x}, \tilde{y}) = \tilde{r}(\tilde{x}, \tilde{y})/\tilde{r}(\tilde{x}, \tilde{x})$, where $\tilde{r}(\tilde{x}, \tilde{y})$ is cross-spectrum density, defined as the temporal Fourier transform of cross-correlation function, $r(x, y) = \lim_{T\to\infty} \int_{-T/2}^{T/2} x(\tau)\, y(\tau + t)\, \mathrm{d}\tau/T$. Source correlation technique reduces the influence of measurement noise. The output signal, s, from the frequency analyzer is a source signal. The stiffness becomes $\tilde{k}_{12} \approx \omega^2 m_b M_{mt} \sum_{n=1}^{M_b} \tilde{h}(\tilde{s}, \tilde{a}_b^n)/[M_b \sum_{p=1}^{M_{mt}} \tilde{h}(\tilde{s}, \tilde{a}_{mt}^p)]$, where a^m is the acceleration at the position m; M_{mt} and M_b are the number of accelerometer positions on the moving table and on the block respectively.

To ensure reliable measurements various blocks are used. Each block mass, including the accelerometer mass on the block and the plate mass, lies in [1·34, 215] kg. The larger the mass the lower the driving point mobility, but, in general, the lower fundamental natural resonance frequency, f_b, is for the block itself. Consequently, heavy blocks are used in the low-frequency region whereas light blocks in the high-frequency region. The frequency range for each block lies in $[N_b f_{ib}, f_b/N_b]$ Hz, where f_{ib} is the axial rigid body resonance frequency of the isolator–block system and N_b is normally greater than 6. Hence, the amplitude and phase errors due to non-vanishing point mobility of the block and non-rigid block motion are negligible. Results from overlapping frequency regions are averaged.

Normally, the static preload on the isolator equals the block static mass. However, the heaviest blocks are suspended by auxiliary rubber isolators, as the model, given in section 2, does not cover the geometrical nor the material non-linearities aligned with finite pre-strains. The actual pre-load never exceeded 500 N.

The experiments are performed at room temperature, $(20{\cdot}9 \pm 0{\cdot}2)^\circ$C. The frequency range considered is 100–5000 Hz. To increase the signal-to-noise ratio, the excitation signal is a stepped sine signal, starting from 100 Hz, with a constant frequency step of 4·5 to 199 Hz, 1 Hz from 200 to 1000 Hz and subsequently, with a step of 4 Hz to 5000 Hz. The signal is recorded within a 5 Hz bandwidth, averaged 5 times and delayed 1000 ms between each recording.

To take the stress softening effects into account, aligned with initial deformations of new rubber samples, also known as Mullins' effect, the test object is preconditioned prior to testing by subjecting to a few deformation cycles at a slow rate in the axial direction with extreme values throughout the cycling, slightly exceeding the actual maximum static pre-load. Dynamic tests are initiated after 1–2 h to allow for stress relaxation.

Each measurement chain—embodying an accelerometer, an accelerometer coaxial cable, a charge amplifier and a RG58 coaxial cable—is sensitivity calibrated in Figure 8(a), with the accelerometer mounted on the shaker table of a calibrated vibration source, B&K 4291. By tuning into the actual accelerometer mass, the built-in generator is adjusted to give a sinusoidal signal with a peak value of 10·0 m/s^2 at 79·6 Hz. The output signal from the charge amplifier is measured by a digital HP 34401A Multimeter. For transfer stiffness measurements it is sufficient to measure the ratio of the block displacement to the moving table displacement; then it is only necessary to determine the relative sensitivity between the measurement chains. Therefore, the calibration discounts any systematic deviation from the stated vibration level of the calibrated vibration source.

Errors due to systematic phase and amplitude mismatch across the channels on the frequency analyzer are reduced in Figure 8(b) by measuring, and gathering, the frequency response functions between them. The output signal from the frequency analyzer is used as a source signal. The frequency range, the frequency step and the time delay are the same as those for stiffness measurements. The number of averages is increased to 50 to minimize random error influence.

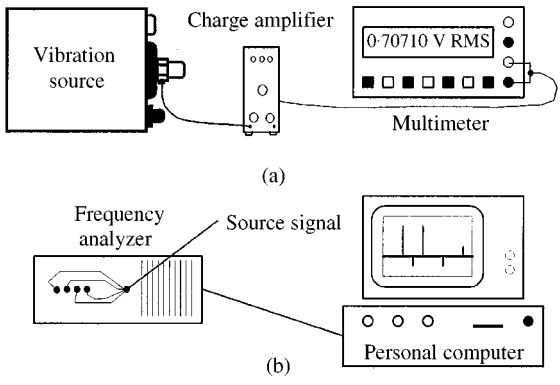

Figure. 8. (a) Sensitivity and (b) cross-channel calibration.

3.2.2. *Measurement results*

The measured axial dynamic transfer stiffness is shown in Figures 9(a)–(d). Figures 9(a) and (b) show the magnitude and the unwrapped phase in the frequency region 100–1000 Hz, while the whole range from 100 to 5000 Hz is shown in Figures 9(c) and (d).

With respect to the magnitude curve in Figure 9(a) and the behaviour of the phase curve in Figure 9(b), the three magnitude peaks most probably correspond to anti-resonances, while the first and third troughs agree with resonances. At an anti-resonance for elastic materials (that is, with no material damping) the stiffness shows a magnitude peak and a phase jump of -180°, while displaying a magnitude trough and a phase jump of $+180^\circ$ at a resonance. Introducing damping, the resonances and anti-resonances are blunted; in general, the magnitude troughs and peaks are rounded, while the sudden phase jumps disappear, showing a "slower" phase shift. Therefore, it may become difficult to distinguish individual resonances and anti-resonances, particularly for high damping material (such as rubber) at closely spaced resonances and anti-resonances.

Confined to the frequency range 1000–5000 Hz, the magnitude curve in Figure 9(c) comprises an oscillating curve, with a rapidly declining amplitude, imposed on a monotonically increasing curve. Likewise, the phase curve in Figure 9(d) oscillates, with rapidly declining amplitude, around -180°. From 4000 to 5000 Hz, the phase curve deviates gradually from -180°. Hitherto, the deviation decreases but is not eliminated, although smaller accelerometers are used and the measurement block is substituted by the bonded steel plate only. The fundamental natural resonance frequency of a *freely* suspended plate rose to 9160 Hz, causing the factor N_b at the high frequency limit to drop to 2. At this stage, the high frequency deviation is most likely due to the plates non-rigid motion.

Regarding measurement noise, the coherence between the source signal and any measurement signal used lies in]0·999900, 1·000000], though rarely lower than 0·999990. The stiffness trough sector at 930 Hz is the frequency region of the lowest coherence. Moreover, the measurement results, including the magnitude and the phase curves, show negligible fluctuations. Accordingly, their measurement quality is excellent.

To sum up, the axial dynamic transfer stiffness is strongly dependent on the frequency. Below 1000 Hz, the stiffness displays definite resonances and anti-resonances, while above 1000 Hz, it compounds from rapidly decaying oscillations on a monotonically increasing curve.

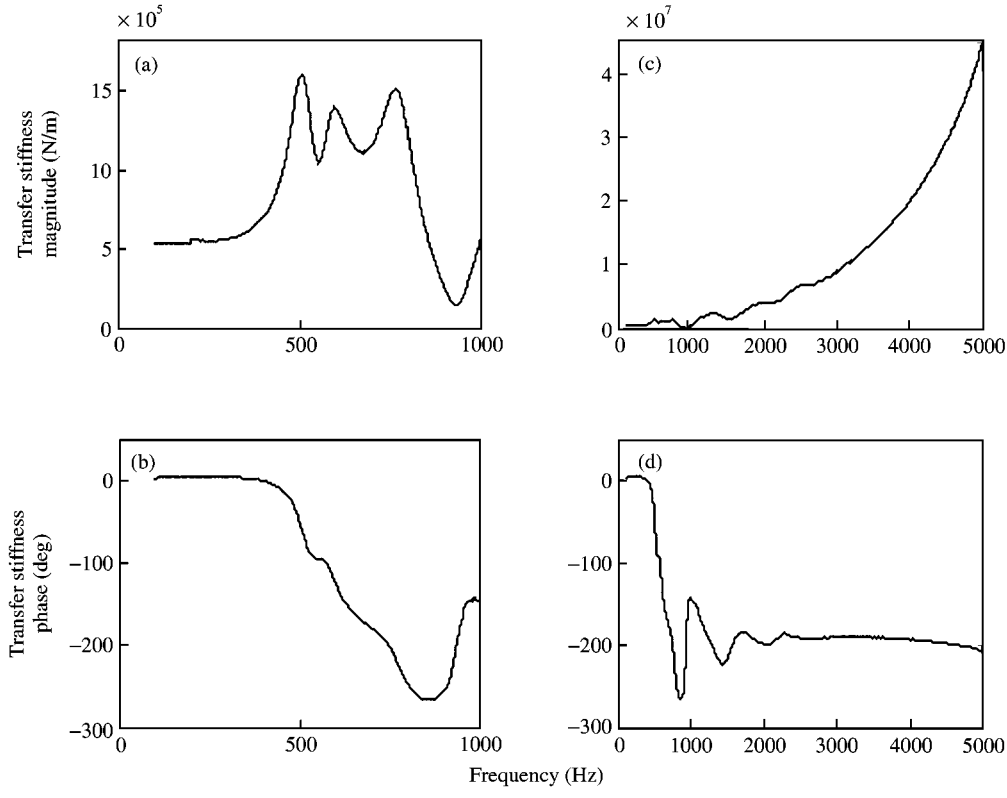

Figure. 9. Measured transfer stiffness. (a) and (b) 100–1000 Hz; (c) and (d) 100–5000 Hz.

3.3. CALCULATED STIFFNESS AND EVALUATION OF MATERIAL MODEL PARAMETERS

Traditionally, material model parameters are calculated from the results of a small test sample undergoing controllable deformation tests. From a practical point of view, the deformation field must be simple to generate, and, in order to obtain accurate results, very well known. Here, for simplicity, the material model parameters are determined from the isolator measured axial dynamic transfer stiffness. Although the field within the cylinder is complicated, the merged axial motion of the plates is simple to generate and measure. It should be noted that this procedure assumes that the presented waveguide solution is correct. This is most likely the case, as shown in Part II. Moreover, a finite element solution [21] at vanishing pre-load, coincides with the presented waveguide solution. This is also the case when varying the material parameters. In order to explore fully the material property influence, other deformation modes may be applied, such as torsion; this is left for future studies, since the focus in this paper is on the axial waveguide solution. In this connection, the transfer stiffness magnitude for the isolator considered displays a strong bulk modulus (or b) dependence for $f > 2000$ Hz. Therefore, the usually laboriously estimated bulk modulus is readily estimated from the transfer stiffness magnitude in the high-frequency region. The use of the present isolator in place of a small test sample enlarges the result's geometrical counterpart. Nevertheless, the effects of variations in the compound ingredients and in component processing are eliminated. Important, but fluctuating processing characteristics are: the temperature and pressure plus the time between the mixing and initiation of cross-linking, the rate of its formation and its extent at the end of the process. In

this connection, bulky rubber samples, such as the isolator considered, are frequently under-vulcanized, compared to small thin-walled rubber samples manufactured from the same mixture.

Regarding the polymer natural rubber, its limited concentration of carbon black and the limited frequency range, a suitable fitting function for the shear modulus is a function with slightly increasing loss factor and magnitude with increasing frequency. It should be emphasized that *any* fitting function is possible, as long as it depicts the observed material behaviour sufficiently accurately within the considered frequency domain, [22]. Here, the fitting function applied is

$$\hat{\mu} = \mu_\infty \left[1 + \frac{(\mathrm{i}\omega\mu_v/\mu_\infty)^{\alpha_2} - (\mathrm{i}\omega\mu_v/\mu_\infty)^{\alpha_1}}{\Delta\alpha \log_e(\mathrm{i}\omega\mu_v/\mu_\infty)} \right], \tag{54}$$

$\Delta\alpha = \alpha_2 - \alpha_1$ is similar to a fractional Kelvin–Voigt model [23], where the equilibrium shear modulus μ_∞ and the parameters μ_v, α_1 and α_2 are to be fitted to the measurement results. Indeed, it reduces to a fractional Kelvin–Voigt model $\hat{\mu} = \mu_\infty\ [1 + (\mathrm{i}\omega\mu_v/\mu_\infty)^\alpha]$, when $\alpha_1, \alpha_2 \to \alpha$. Note that the Fourier transform of the fractional derivative of order α of $x(t)$ is $(\mathrm{i}\omega)^\alpha$ times the Fourier transform of $x(t)$ [9]. The corresponding relaxation function to the fitting function reads

$$\mu(t) = \mu_\infty \left[h(t) + \frac{1}{\Delta\alpha} \int_{\alpha_1}^{\alpha_2} (\mu_v/\mu_\infty)^\alpha I_\alpha(t)\, \mathrm{d}\alpha \right], \tag{55}$$

where the Abel operator kernel $\mathrm{I}_\alpha(t) = h(t)/[t^\alpha \Gamma(1-\alpha)]$, [23], and Γ is a Gamma function [20], $\Gamma(z) = {}_0\int^\infty s^{z-1}\mathrm{e}^{-s}\,\mathrm{d}s$, $z > 0$, reducing to a relaxation function of a fractional Kelvin–Voigt model $\mu(t) = \mu_\infty[h(t) + (\mu_v/\mu_\infty)^\alpha \mathrm{I}_\alpha(t)]$, when $\alpha_1, \alpha_2 \to \alpha$.

Estimated bulk modulus is readily estimated from the transfer stiffness magnitude in the high-frequency region.

The material parameters in equation (54) were fitted manually. Principally, the equilibrium shear modulus μ_∞ in addition to μ_v, α_1 and α_2 was determined by fitting the low-frequency region of the transfer stiffness curve ($f < 300$ Hz) to measurements while the corresponding high-frequency region ($f > 2000$ Hz) determined b. The parameters were then slightly adjusted to give a good overall fit throughout the whole frequency region. The rubber density was provided by the rubber manufacturer. The "least squares" estimated parameters are: $\mu_\infty = 5{\cdot}94 \times 10^5$ N/m^2, $\mu_v = 13{\cdot}0$ Ns/m^2, $\alpha_1 = 0{\cdot}080$, $\alpha_2 = 0{\cdot}625$ and $b = 2{\cdot}22 \times 10^3$, together with $\rho = 1050$ kg/m^3. The estimated parameters are realistic: the equilibrium Poisson ratio is 0·4998, the density equals the stated value, while the equilibrium bulk and shear moduli slightly exceed the stated values. The shear modulus in the extended frequency range 1–10 000 Hz is in Figure 10, showing a slight magnitude and loss factor increase with increasing frequency, as expected. The bulk modulus is a constant; $1{\cdot}32 \times 10^9$ N/m^2. It should be noted that the applied fitting function is sufficient within the considered frequency domain, while considerably higher frequencies require other models, such as a fractional standard linear (or three element) solid [23], showing a finite glass modulus.

The calculated stiffness is determined by point matching, using equidistant collocation radii, $P_r^1 = P_z^1 = P_r^2 = P_z^2 = 100$ and $M = 100$; the equation system is, therefore, overdetermined. The frequency points coincide with the measurement points. For all frequencies considered, the effective rank of system matrix $\mathbf{A}'$ is full, that is 200.

The calculated stiffness is in Figures 11 and 12. Figures 11(a)–(e) show the transfer stiffness. Figures 12(a)–(f) show the driving point stiffness. In addition and for comparison,

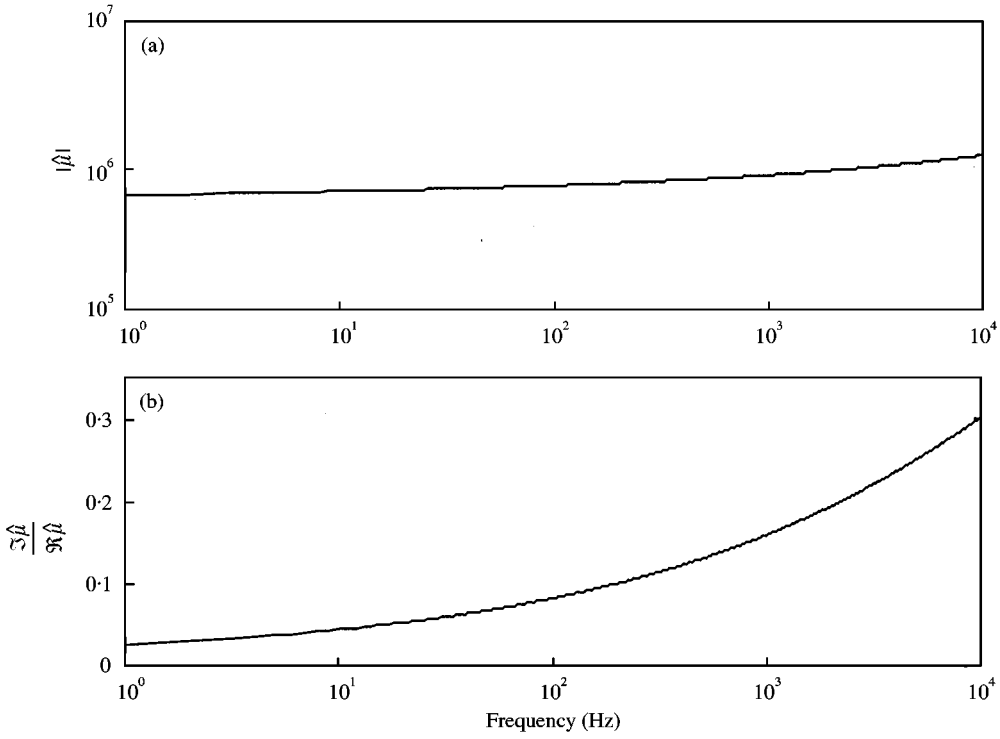

Figure. 10. Shear modulus. 1–10 000 Hz. (a) Magnitude and (b) loss factor.

the results of the axial transfer stiffness measurement are shown in Figures 11(a)–(e). The curves from the measurement are plotted in dashed lines while those from the calculations are solid.

The measured and calculated axial transfer stiffness agree very well. In particular, the low- frequency plateau, the peaks and the troughs in Figure 11(a) are almost exactly reproduced. In Figure 11(b), the calculated phase corresponds to the measured phase with only minor discrepancies. The low-frequency fragment of the phase curve shown in Figure 11(c) results mainly from the material properties in shear. For comparison, the phase curve of the shear modulus is plotted in a dash-dotted line closely following the phase curve of the dynamic stiffness to 150 Hz. The ensuing deviations are mainly due to geometrical effects. Apparently, it is possible to achieve a good fit of the material damping of the applied nearly incompressible material model embodying a simple fitting function, to those of measurements. Magnitude and phase curves in the whole frequency region of 50–5000 Hz are shown in Figures 11(d) and (e), where measurements and calculations match very well. The small deviations close to 5000 Hz, slightly more conspicuous for the phase, result most probably from non-rigid plate motions (or from a possible anti-resonance in the high-frequency region).

The driving point stiffness depends upon the dynamic properties of the plates in section 3.1. Three isolator plate configurations are provided in Figures 12(a)–(f), plates not included are plotted in solid lines, 2·6 mm plates included are plotted in dotted lines and (2·6 + 19·0) mm plates included are plotted in dash-dotted lines.

With reference to the magnitude curve in Figure 12(a) and the behaviour of the phase curve in Figure 12(c), the three magnitude peaks, without plates (that is, $\rho_{mp} \equiv 0$), most

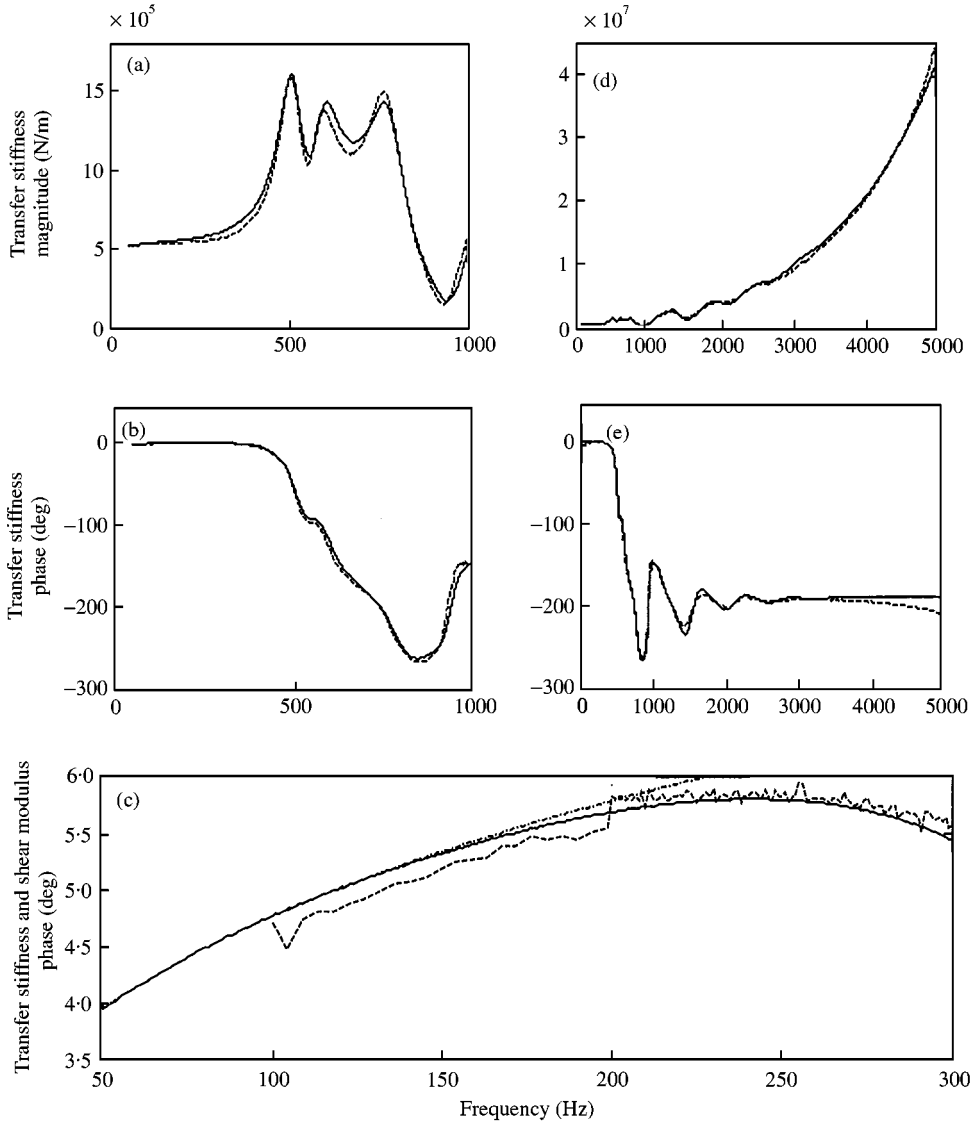

Figure. 11. Calculated (solid) and measured (dashed) transfer stiffness. (a) and (b) 50–1000 Hz; (c) 50–300 Hz, shear modulus (dash-dotted); (d) and (e) 50–5000 Hz.

likely correspond to anti-resonances, while the four troughs agree with resonances. Incorporating the plates, the stiffness reads $\tilde{k}_{11} = \tilde{k}_{11}|_{no\ plates} - \omega^2 m_{mp}$, where m_{mp} is the plate mass. In Figure 12(b), although more definite in Figure 12(c), the first resonance is shifted to 190 and 90 Hz, respectively, for 2·6 mm and (2·6 + 19·0) mm plates. Subsequently, the dotted and the dash-dotted magnitude curves exceed the solid curve, more conspicuously with (2·6 + 19·0) mm plates.

Next, the driving point stiffness in the whole frequency region of 50–5000 Hz is in Figures 12(d)–(f), where stiffness oscillates slightly, but tends towards $-\omega^2 (m_{mp} + m_{eff})$ for higher frequencies, with m_{eff} as cylinder effective mass. Physically, the effective mass can be considered as the equivalent part of the rubber mass moving in parallel with $\partial_d^1 \mathscr{B}$; here, being $\sim$40% at 5000 Hz.

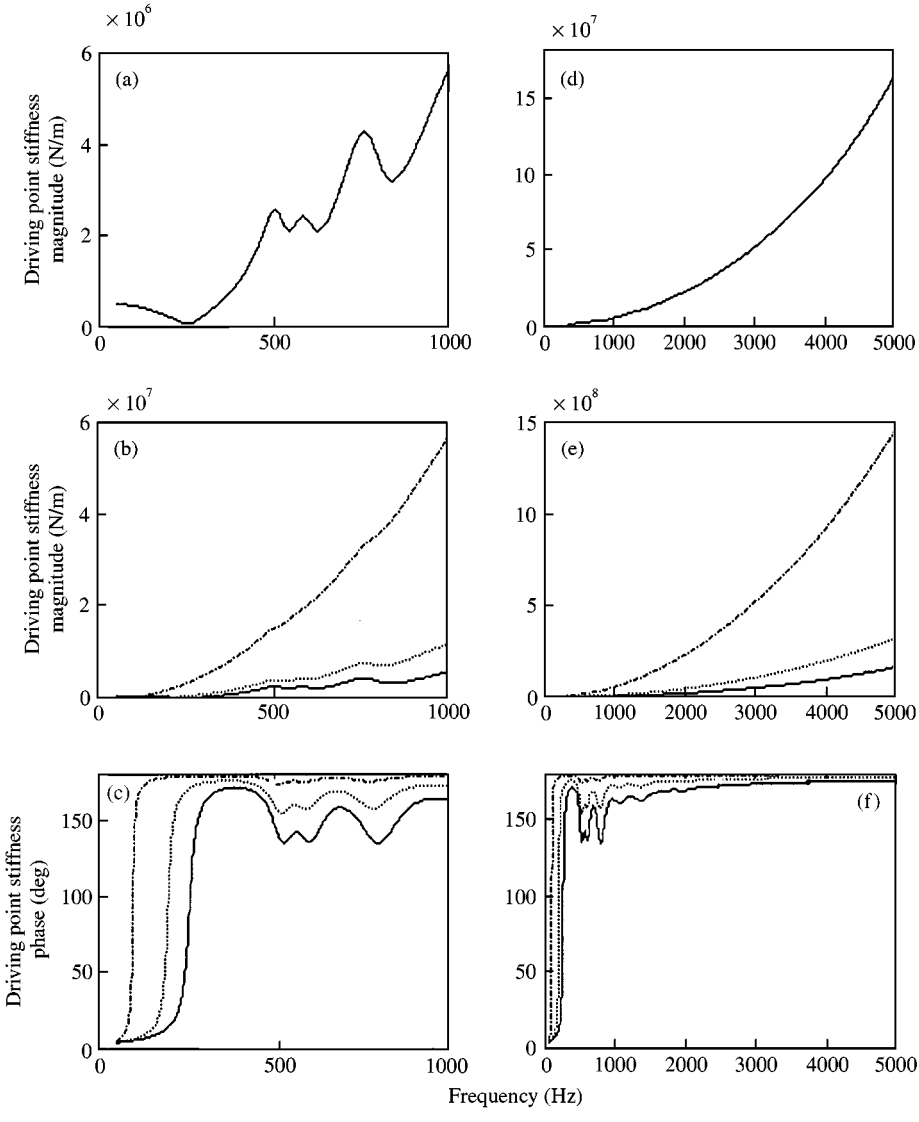

Figure. 12. Calculated driving point stiffness. Bonded steel plates not included (solid), 2·6 mm (dotted) and (2·6 + 19·0) mm bonded steel plates included (dash-dotted). (a), (b) and (c) 50–1000 Hz; (d), (e) and (f) 50–5000 Hz.

Finally, the stiffness in the extended frequency region of 50–10 000 Hz is shown in Figures 13(a)–(d), displaying a lightly damped anti resonance at 8600 Hz. To obtain satisfactory results close to this frequency the total mode number is increased to $M = 256$ while $P_r^1 = P_z^1 = P_r^2 = P_z^2 = 256$. The magnitude ratio of maximum to minimum stiffness within the frequency range is roughly 10^4 to 10^5, which definitely alters the definition of "spring constant".

3.3.1. *Other material models*

In order to study further the material model significance for the stiffness, two typical material models are applied to the nearly incompressible model. The parameters are

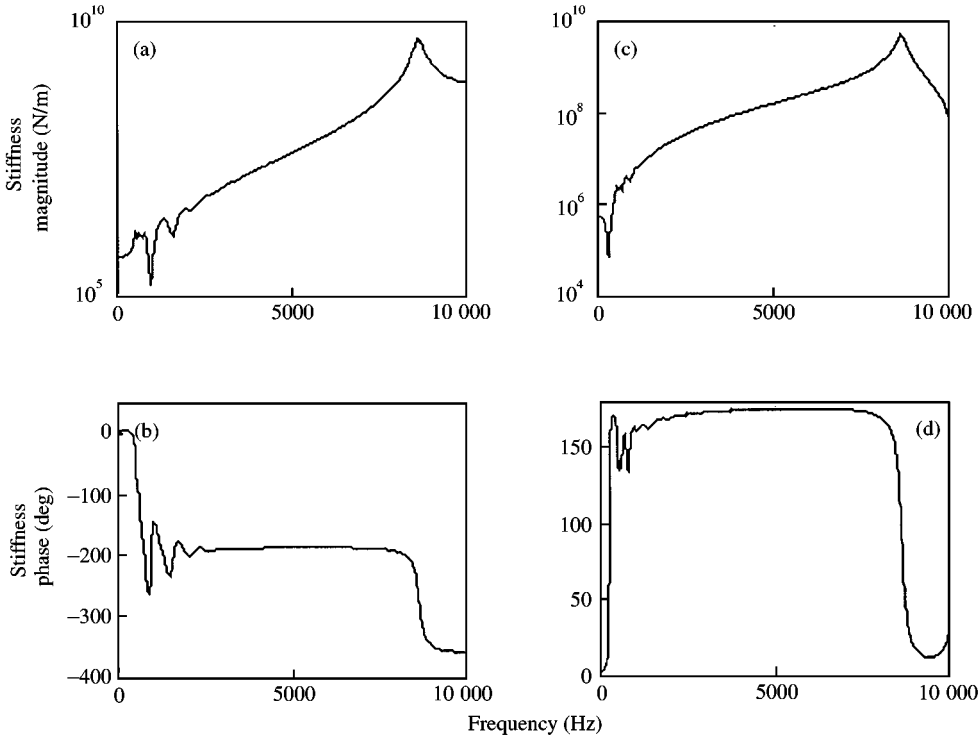

Figure. 13. Calculated (a) and (b) transfer stiffness; (c) and (d) driving point stiffness. Bonded steel plates not included; 50–10 000 Hz.

adjusted so as to be equal in density, bulk modulus, equilibrium shear modulus and the loss factor of shear modulus (at 100 Hz), used as in the current model (54), resulting in equal static stiffness and measurement coincident stiffness phase at 100 Hz. In Figure 14, the stiffness due to the frequency independent shear modulus, $\hat{\mu} = \mu_\infty(1 + 8{\cdot}35 \times 10^{-2}\,\mathrm{i})$, and the ordinary Kelvin–Voigt model, $\hat{\mu} = \mu_\infty\,(1 + 8{\cdot}35 \times 10^{-4}\,f\mathrm{i})$, are plotted in dotted and dash-dotted lines, respectively. The frequency range is 50–1000 Hz. The driving point stiffness is shown in Figures 14(c) and (d), while the transfer stiffness is shown in Figures 14(a) and (b). For comparison, the measurement results for the transfer stiffness is shown in Figure 14(a) and (b), plotted as a dashed line. In addition, the previously determined stiffness is shown in a solid line, with its shear modulus displayed in Figure 10. Clearly, the simple models fail to model the stiffness satisfactorily. The shear modulus is, for both models, underestimated in the frequency range considered resulting in an underestimation of the magnitude of the low-frequency stiffness and a shift of the resonance and anti-resonance frequencies to lower frequencies. In addition, the Kelvin–Voigt model overestimates the material damping in the high-frequency region ($f > 100$ Hz), while the frequency-independent model underestimates it. The peaks are, therefore, sharper for the frequency-independent model and heavily broadened for the Kelvin–Voigt model. It is possible to adjust the equilibrium shear moduli to give better low-frequency stiffness magnitude agreements; this would however result in unrealistic large (erroneous) equilibrium shear moduli. Other material models, such as the fractional standard linear (or three element) solid [23], were tested but the fitting function applied to the nearly incompressible model is superior in this study. To enhance further the high-frequency

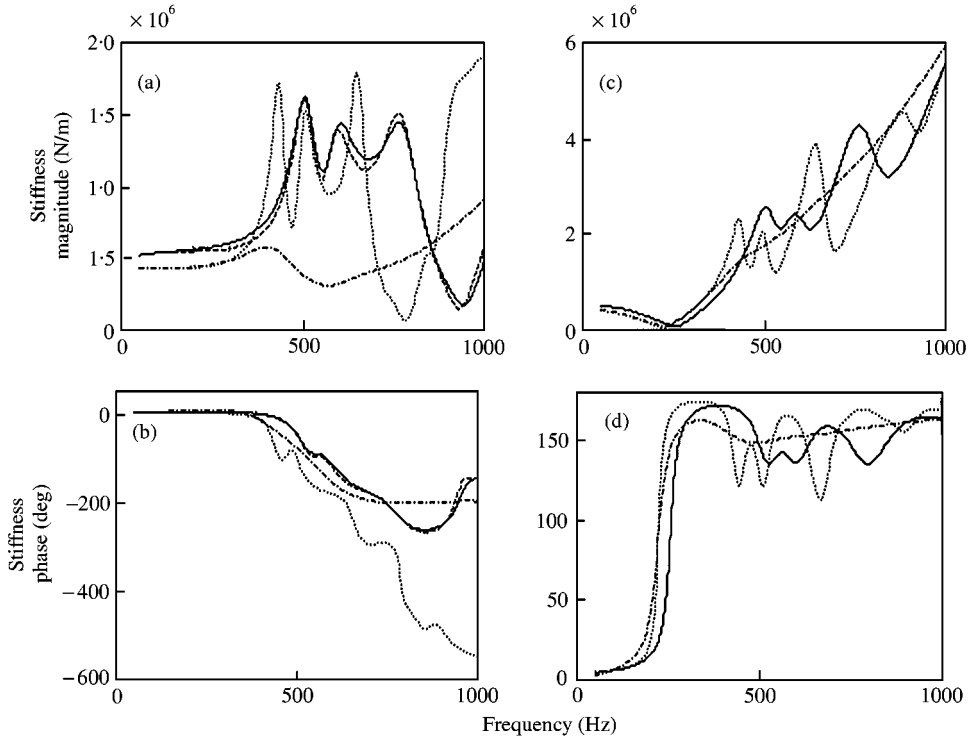

Figure. 14. Calculated (a) and (b) transfer stiffness; (c) and (d) driving point stiffness. Measurement (dashed); present (solid thick), frequency independent (dotted) and Kelvin–Voigt model (dash-dotted). Bonded steel plates not included; 50–1000 Hz.

stiffness phase agreement with measurements for $f > 1000$ Hz, the bulk response may be viscoelastically modelled rather than purely elastically.

4. CONCLUSIONS

In presenting a linear axial dynamic stiffness model for cylindrical vibration isolators over an audible frequency range of particular complexity and interest in noise abatement, the problems of simultaneously satisfying the boundary conditions at the lateral and radial surfaces of the cylinder are removed. The remedy is to satisfy approximately the boundary conditions at the lateral surfaces by a circle-wise fulfilment or a subregion method and by adopting the mode-matching technique while using the dispersion relation for an infinite cylinder. The rubber material is modelled as nearly incompressible with deviatoric viscoelasticity based on a fractional order derivative model. The main advantage of the viscoelastic model is the minimum parameter number required to model the material properties successfully over a broad structure-borne sound frequency domain. The work is verified by experiments on a rubber cylinder, equipped with bonded circular steel plates, in the frequency range 100–5000 Hz. The model and the measurements are shown to be in striking agreement within the whole frequency range. Comparisons with alternative material models are made, known as the Kelvin–Voigt and frequency independent or "hysteric" material models. The results are shown to diverge substantially from the presented material model; in particular, the Kelvin–Voigt model overestimates the material damping in the high-frequency region,

while the frequency-independent model underestimates it. In addition, the resonance and anti resonance frequencies are incorrectly predicted. In a companion paper [10] the dispersion relation solution, convergence analysis and comparison with simple models are addressed.

To derive other components of dynamic stiffness with methods similar to those presented is an interesting continuation of this work.

REFERENCES

1. G. M. L. GLADWELL and D. K. VIJAY 1975 *Journal of Sound and Vibration* **42**, 137–145. Vibration analysis of axisymmetric resonators.
2. G. M. L. GLADWELL and U. C. TAHBILDAR 1972 *Journal of Sound and Vibration* **22**, 143–157. Finite element analysis of the axisymmetric vibrations of cylinders.
3. G. W. MCMAHON 1970 *Journal of the Acoustical Society of America* **48**, 307–312. Finite-difference analysis of the vibration of solid cylinders.
4. L. GAUL 1991 *Mechanical Systems and Signal Processing* **5**, 13–24. Dynamic transfer behaviour of elastomer isolators; boundary element calculation and measurements.
5. J. ZEMANEK JR 1972 *Journal of the Acoustical Society of America* **51**, 265–283. An experimental and theoretical investigation of elastic wave propagation in a cylinder.
6. D. J. EWINS 1991 *Modal Testing*: *Theory and Practice*, Reprint. Letichwar Research Studies Press. ISBN 0-86380-017-3.
7. S. H. CRANDALL 1963 in *Air Space and Instruments*, *Draper Anniversary Volume* (S. Lees, editor) 183–193. New York: McGraw-Hill. BNB 99-119698-4. Dynamic response of systems with structural damping.
8. R. M. CHRISTENSEN 1982 *Theory of Viscoelasticity* Academic Press. ISBN 0-12-174252-0; Second Edition.
9. R. L. BAGLEY and P. J. TORVIK 1983 *American Institute of Aeronautics and Astronautics Journal* **21**, 741–748. Fractional calculus—A different approach to the analysis of viscoelastically damped structures.
10. L. KARI 2001 *Journal of Sound and Vibration* **244**, 235–257. On the waveguide modelling of dynamic stiffness of cylindrical vibration isolators. Part II: the dispersion relation solution, convergence analysis and comparison with simple models (accepted for publication).
11. Y. C. FUNG 1965 *Foundations of Solid Mechanics*. Englewood Cliffs, NJ: Prentice-Hall. ISBN 0-13-329912-0.
12. J. MIKLOWITZ 1984 *The Theory of Elastic Waves and Waveguides*. Amsterdam: North-Holland. ISBN 0-444-87513-1.
13. R. MITTRA and S. W. LEE 1971 *Analytical Techniques in the Theory of Guided Waves*. New York: MacMillan Company. LCC Card Number 70-116784.
14. K. F. GRAFF 1991 *Wave Motion in Elastic Solids*. New York: Dover Publications. pp. 470–472. Chapter 8.2, ISBN 0-486-66745-6.
15. L. POCHHAMMER 1876 *Journal für die reine und angewandte Mathematik* **81**, 324–336. Über die Fortpflanzungsgeschwindigkeiten kleiner Schwingungen in einem unbegrenzten isotropen Kreiszylinder.
16. C. CHREE 1889 *Transactions of the Cambridge Philosophical Society* **14**, 250–369. The equations of an isotropic elastic solid in polar and cylindrical coordinates, their solutions and applications.
17. A. E. H. LOVE 1927 *A Treatise on the Mathematical Theory of Elasticity*. Cambridge: Cambridge University Press; fourth edition.
18. J. ADEM 1954 *Quarterly of Applied Mathematics* **12**, 261–275. On the axially-symmetric steady wave propagation in elastic circular rods.
19. M. CESSENAT 1996 *Mathematical Methods in Electromagnetism*. Singapore: World Scientific. ISBN 981-02-2467-2.
20. M. ABRAMOWITZ and I. A. STEGUN 1972 *Handbook of Mathematical Functions*. New York: Dover Publications. ISBN 0-486-61272-4. Ninth Printing.
21. L. KARI 1999 *Proceedings of the Sixth International Congress on Sound and Vibration* (Ed. Finn Jacobsen), pp. 2081–2090. The audible stiffness of preloaded vibration isolators.
22. K. DOVSTAM 1997 *Personal communication*.
23. R. C. KOELLER 1984 *Transactions of the American Society of Mechanical Engineers Journal of Applied Mechanics* **51**, 299–307. Applications of fractional calculus to the theory of viscoelasticity.